ACS APPLIED MATERIALS & INTERFACES

Research Article

www.acsami.org

Magnetic Iron Oxide Chestnutlike Hierarchical Nanostructures: Preparation and Their Excellent Arsenic Removal Capabilities

Fangzhi Mou, Jianguo Guan,* Huiru Ma, Leilei Xu, and Weidong Shi

State Key Laboratory of Advanced Technology for Materials Synthesis and Processing, Wuhan University of Technology, Wuhan 430070, P. R. China

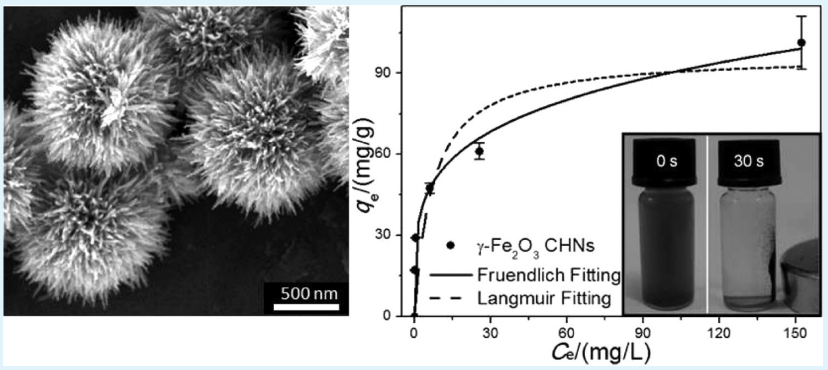

ABSTRACT: To obtain adsorbents with high As(V) removal capacity and quick magnetic separation simultaneously, we have fabricated maghemite (γ-Fe_2O_3) and magnetite (Fe_3O_4) chestnutlike hierarchical nanostructures (CHNs) with strong ferromagnetic property by annealing the Fe_2O_3 chestnutlike amorphous core/γ-phase shell hierarchical nanoarchitectures (CAHNs) at different temperatures in a nitrogen atmosphere. Compared to the Fe_2O_3 CAHNs, the saturated magnetization of the as-obtained γ-Fe_2O_3 CHNs is enhanced over 10 times, while the As(V) removal capacity is maintained 74% and reaches 101.4 mg·g^{-1}. Both of the as-obtained γ-Fe_2O_3 and Fe_3O_4 CHNs can be separated simply and rapidly from treated water by magnetic separation after As(V) adsorption treatment. The As(V) adsorption process of the as-obtained γ-Fe_2O_3 CHNs obeys well the Freundlich isotherm model rather than the Langmuir one, suggesting that a multilayered adsorption occurs on the surface of the γ-Fe_2O_3 CHNs. Taking advantages of the high adsorption capacity, fast adsorption rate and quick magnetic separation from treated water, the γ-Fe_2O_3 CHNs developed in the present study is expected to be an efficient magnetic adsorbent for As(V) removal from aqueous solutions.

KEYWORDS: *iron oxide, magnetic properties, hierarchical nanostructures, arsenic adsorption, water treatment*

INTRODUCTION

Arsenic pollution in water has attracted worldwide attention because of its high toxicological effects on human body.[1−3] To eliminate arsenic pollutants from drinking water, numerous technologies, such as oxidation,[4,5] coagulation,[6] adsorption,[7,8] ion-exchange, and reverse osmosis,[9] have been developed. Among them, adsorption has obviously advantages such as better performance, easy operation, and lower cost.[3]

As an ideal adsorbent for the removal of toxic ions in water, magnetic adsorbents may exhibit quick and effective magnetic separation from treated water. This unique property can overcome some of the issues present in filtration, centrifugation or gravitational separation, and save energy.[10,11] However, magnetic maghemite (γ-Fe_2O_3) and magnetite (Fe_3O_4) nanoparticles with size about 3.8 and 12 nm, respectively, which both show promising As(V) removal capacities,[10,12,13] are increasingly difficult to separate from water even under a high magnetic field of 5000 Oe.[10,14] This is because the magnetic response of a magnetic adsorbent decreases undesirably in water as its size decreases. Magnetic hierarchical nanostructures (HNs), which are constructed by building blocks of nanoparticles,[15] nanoplates[16] or nanorods[17,18] etc., not only exhibit a high specific surface areas because of the abundant interparticle spaces or intraparticle pores resulting from their complex structure, but also are more easily separated because of their larger size, weaker Brownian motion, and better magnetic properties compared to nanosized powder adsorbents.[14,19−21] However, the 3D flowerlike magnetic γ-Fe_2O_3 and Fe_3O_4 HNs reported previously have relatively low surface area and only show adsorptive capacities for As(V) as low as 4.75 and 4.65 mg·g^{-1} at pH 4, respectively.[22]

By combining the high surface area of amorphous Fe_2O_3 and fine magnetic property of γ-Fe_2O_3, we have successfully developed a magnetic adsorbent of Fe_2O_3 chestnutlike amorphous core/γ-phase shell hierarchical nanoarchitectures (CAHNs) for As(V) removal, which showed an extraordinary

Received: May 10, 2012
Accepted: July 13, 2012
Published: July 13, 2012

As(V) removal capability (137.5 mg·g^{-1}).[23] Because of the existence of amorphous Fe_2O_3 core, however, the Fe_2O_3 CAHNs show a low saturation magnetization (M_s) (2.1 emu·g^{-1} at 10 kOe). This severely limits the sensitivity to the applied magnetic field and magnetic separation rate.

To significantly enhance the M_s of the CAHNs, we have fabricated strong magnetic γ-Fe_2O_3 and Fe_3O_4 chestnutlike hierarchical nanostructures (CHNs) by simply annealing the Fe_2O_3 CAHNs at different temperatures under nitrogen atmospheres. The resultant γ-Fe_2O_3 CHNs exhibit a high As(V) removal capability and rapid magnetic separation.

EXPERIMENTAL SECTION

Preparation of γ-Fe_2O_3 and Fe_3O_4 CHNs. The Fe_2O_3 CAHNs, denoted as the precursor, were first prepared through a solvothermal reaction which was reported elsewhere.[23] Briefly, 80 mL of *N*,*N*-dimethyllformamide (DMF) solution contained 0.24 mmol $SnCl_2{\cdot}2H_2O$ and 0.5 mL $Fe(CO)_5$ was transferred into a 100 mL Teflon-lined stainless steel autoclave, and then sealed and maintained at 200 °C for 8 h. After being cooled to room temperature, the brown product was isolated by centrifugation, repeatedly washed with absolute ethanol several times and dried in vacuum at 40 °C for 8 h, and then the precursors of Fe_2O_3 CAHNs were obtained. To obtain γ-Fe_2O_3 and Fe_3O_4 CHNs, the Fe_2O_3 CAHNs were annealed at 300 and 500 °C under protection of N_2 for 4 h, respectively.

Characterization. Scanning electron microscopy (SEM) images were obtained using a Hitachi S-4800 (Japan) field-emission scanning electron microscope. The X-ray diffraction (XRD) patterns of the Fe_2O_3 CAHNs and the γ-Fe_2O_3 and Fe_3O_4 CHNs were obtained by using Rigaku D/Max-RB diffractometer at a voltage of 40 kV and a current of 200 mA with Cu−Kα radiation (λ = 0.15406 nm). The scanning rate is 4°·min^{-1} and scanning step is 0.02° in the 2θ range of 15 to 80°. A micro-Raman study was performed on the Reinshaw inVia (Britain) laser confocal Raman microscope at room temperature under the excitation of 514.5 nm wavelength of an Ar^+ laser. The laser power was limited to 0.5 mW to avoid possible phase transition during the laser irradiation. Magnetic measurements for the samples in the powder form were carried out using a model 4HF vibrating sample magnetometer (VSM, ADE Co. Ltd., USA) with a maximum magnetic field of 10 kOe. The Brunauer−Emmett−Teller (BET) surface area of the samples was analyzed by nitrogen adsorption on a Micromeritics ASAP 2020 nitrogen adsorption apparatus (USA). All the samples were degassed at 150 °C prior to nitrogen adsorption measurements. The specific surface area was determined by a multipoint BET method using the adsorption data in the relative pressure (P/P_0) range of 0.05−0.25. Desorption isotherm was used to determine the pore size distribution using the Barret−Joymer−Halender method. The nitrogen adsorption volume at the relative pressure (P/P_0) of 0.970 was used to determine the pore volume and porosity.

Adsorption of As (V) Experiments. For the adsorption kinetics of As(V), solutions with As(V) concentrations of 6.96 mg·L^{-1} were first prepared using $Na_3AsO_4{\cdot}12H_2O$ as a source of As(V) and adjusted pH = 4 with HCl or NaOH. Then, 0.02 g of the adsorbent sample was added to 50 mL of the above solution under stirring. The adsorbents were separated from the solution by magnetic separation after a specified time, and inductively coupled plasma-atomic emission spectroscopy (ICPAES, Perkin-Elmer Optima 4300DV) was used to measure the arsenic concentration in the remaining solutions. The equilibrium-sorption capacity (q_e) was calculated from eq 1

$$q_e = \frac{(C_0 - C_e)V}{m} \quad (1)$$

where C_0 and C_e represent the concentration of As(V) before and after removal process, respectively; V is the solution volume and m the weight of the adsorbent.[24] To obtain the adsorption isotherm, 0.01 g of Fe_2O_3 CAHNs or γ-Fe_2O_3 CHNs was added into 25 mL of the As(V) aqueous solution with C_0 from 6.96, 12, 25, 50, 100, and 182.5 to 200 mg·L^{-1} and stirred for 3 h at room temperature (25.0 ± 1.0 °C), respectively. The solid and liquid phases were then magnetically separated and the arsenic concentration in the remaining solutions was measured by the ICPAES.

RESULTS AND DISCUSSION

Figure 1A shows that the as-prepared Fe_2O_3 CAHNs have a chestnutlike morphology and are nearly uniform with the

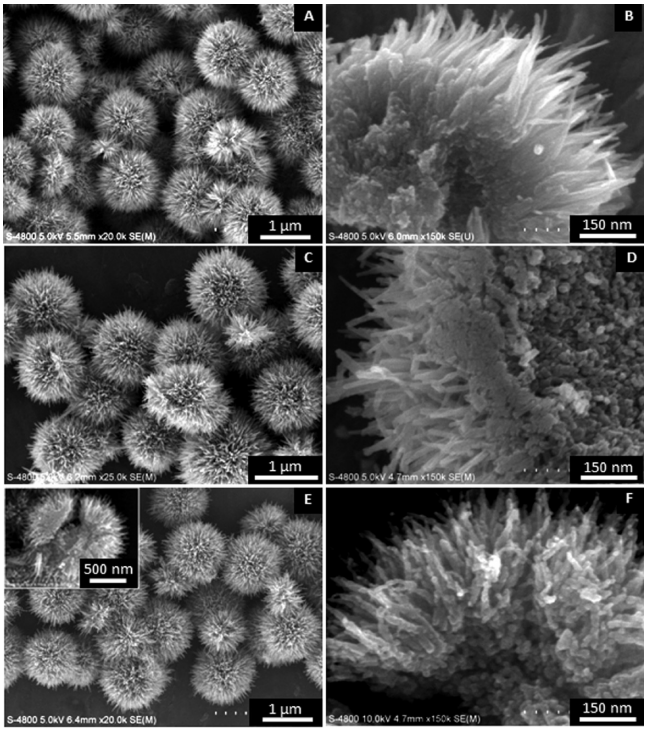

Figure 1. SEM images of the Fe_2O_3 CAHNs (A, B), and the products obtained by calcining the Fe_2O_3 CAHNs at 300 (C, D) and 500 °C (E, F) under protection of N_2 for 4 h, respectively. B, D, and F show the SEM images of the corresponding cracked structures.

diameters of about 1.5 μm. The magnified SEM image of a typical broken nanostructure is shown in Figure 1B, which clearly indicates that the entire architecture consists of a solid core and radially grown nanorods. The nanorods show a smooth surface and sharp tip with about 20 nm in diameters and 300 nm in lengths. The SAED pattern captured at the spherical core and HRTEM images captured at the nanorod on the surface of Fe_2O_3 CAHNs have confirmed that the Fe_2O_3 CAHNs have an amorphous core/γ-phase shell chestnutlike hierarchical structure in our previous study.[23]

Figure 1C−F show that the samples obtained by respectively calcining the Fe_2O_3 CAHNs at 300 and 500 °C both maintain their original chestnutlike morphologies and diameters of the precursors. To obtain the information of the internal structures, we slightly pressed the products before SEM characterization. The typical broken nanostructure of the product obtained at 300 °C is shown in Figure 1D, and that obtained at 500 °C is shown in the inset of Figure 1E and Figure 1F. The products show a clear core/shell nanostructure, in which the core is comprised of nanoparticles and the shell consists of radially grown nanorods. Close observation reveals that the interior nanoparticles of the product obtained at 300 °C have an average size of 12 nm, which is smaller than that of the product obtained at 500 °C (20 nm). The nanorods on the surface of the product obtained at 300 °C show uniform and smooth

surfaces, while those at 500 °C are highly melted with rougher surfaces.

The XRD patterns of the Fe_2O_3 CAHNs and the products obtained by calcining Fe_2O_3 CAHNs at 300 and 500 °C are shown in Figure 2. The XRD pattern of the Fe_2O_3 CAHNs

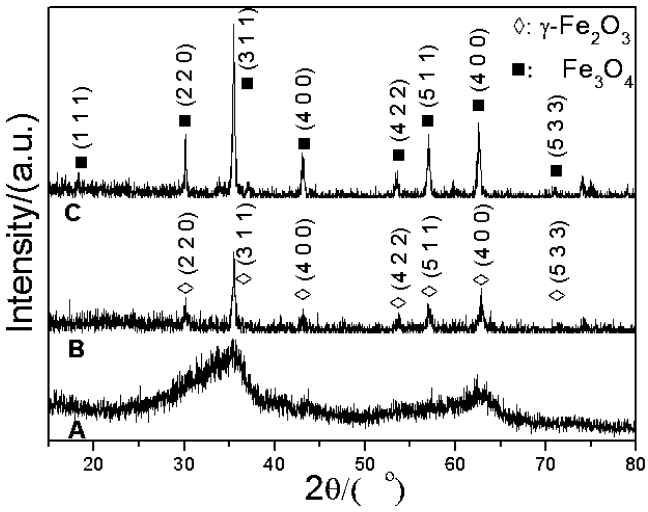

Figure 2. XRD patterns of the Fe_2O_3 CAHNs (A) and the products obtained by calcining the Fe_2O_3 CAHNs at 300 (B) and 500 °C (C) under protection of N_2 for 4 h, respectively.

(Figure 2A) has two broad peaks located at 35.6° and 62.9° because of their unique amorphous core/γ-phase shell nanostructures. After the Fe_2O_3 CAHNs are annealed at elevated temperature under protection of N_2 for 4 h, the reddish brown product was obtained. Meanwhile, the broad XRD peaks of the Fe_2O_3 CAHNs are transformed into sharp ones after the calcination owing to the crystallization of the Fe_2O_3 amorphous core. Figure 2B and C indicate that the products obtained at 300 and 500 °C both have the similar XRD patterns, in good agreement with the pure γ-Fe_2O_3 or Fe_3O_4 (Maghemite, JCPDS No. 39-1346 or Magnetite, JCPDS 19-0629). Because the maghemite and magnetite have a similar XRD pattern, Raman spectroscopy was carried out to confirm the crystalline structure of the products obtained at elevated temperatures after heavily grinding. Figure 3 shows that the Raman spectrum of the products obtained at 300 °C is similar to that of Fe_2O_3 CAHNs. The Raman peaks at 368, 496, and 700 cm^{-1} are observed, which are consistent with the E_g, T_{2g}, and $A_{1\,g}$ modes of inverse spinel structure γ-Fe_2O_3.[25−27] This indicates that the crystalline structure of the products obtained at 300 °C is γ-Fe_2O_3. For the products obtained at 500 °C, the Raman spectrum (Figure 3C) presents three bands at 297, 538, and 662 cm^{-1}. This further confirms that they are Fe_3O_4.[25] Figure 4 shows that there is 9.42 wt % of carbon presented in the Fe_2O_3 CAHNs. Therefore, the formation of Fe_3O_4 can be ascribed to the reducing ability of carbon during the heat treatment.[23]

The room temperature magnetic hysteresis loops of the Fe_2O_3 CAHNs, γ-Fe_2O_3, and Fe_3O_4 CHNs are shown in Figure 5. The nonlinear hysteresis loops with nonzero remnant magnetization (M_r) and coercivity (H_c) show well pronounced ferromagnetic properties of the various iron oxide chestnutlike core/shell nanostructures. The M_s for the γ-Fe_2O_3, Fe_3O_4 CHNs is 22.1 and 69.97 emu·g^{-1}, corresponding to about 10 and 30 times higher than that of the Fe_2O_3 CAHNs (2.1

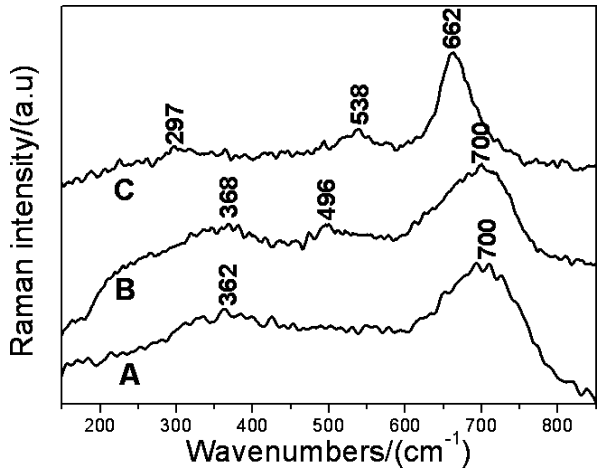

Figure 3. Raman spectra of the Fe_2O_3 CAHNs (A) and the products obtained by calcining the Fe_2O_3 CAHNs at 300 (B) and 500 °C (C) under protection of N_2 for 4 h, respectively.

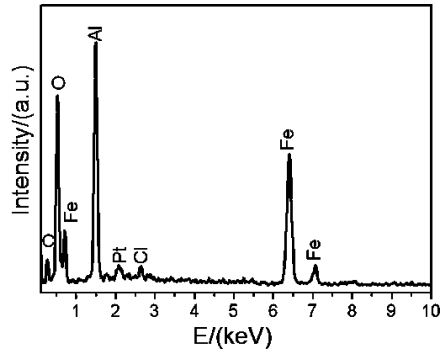

Figure 4. EDX analysis of the Fe_2O_3 CAHNs; the peaks of Al, Pt, and Cl in the EDX pattern are caused by the signals generated from the used Al substrate, the Pt coating during the SEM test, as well as the adsorbed chloride ions existed in the reaction system, respectively.

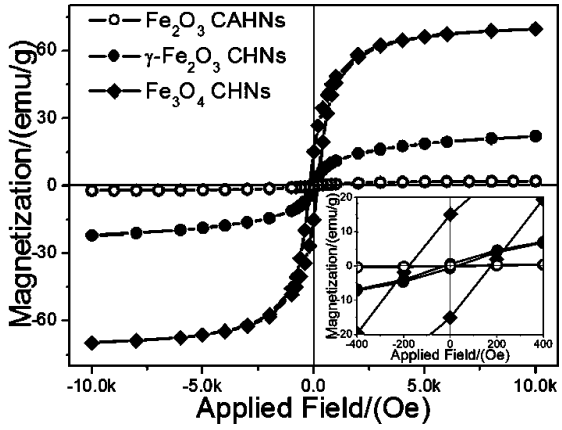

Figure 5. Room temperature hysteresis loops for the Fe_2O_3 CAHNs, γ-Fe_2O_3, and Fe_3O_4 CHNs, respectively.

emu·g^{-1}), respectively. This implies that the relatively strong magnetic response of the annealed CHNs to the external magnetic field. The M_s for the as-prepared γ-Fe_2O_3 and Fe_3O_4 CHNs is lower than that of the corresponding bulk ones (80 emu·g^{-1} for γ-Fe_2O_3[28] and 92 emu·g^{-1} for Fe_3O_4[29]). A decrease in M_s is usually observed in nanostructures and can be attributed to the surface contribution: spin canting, surface

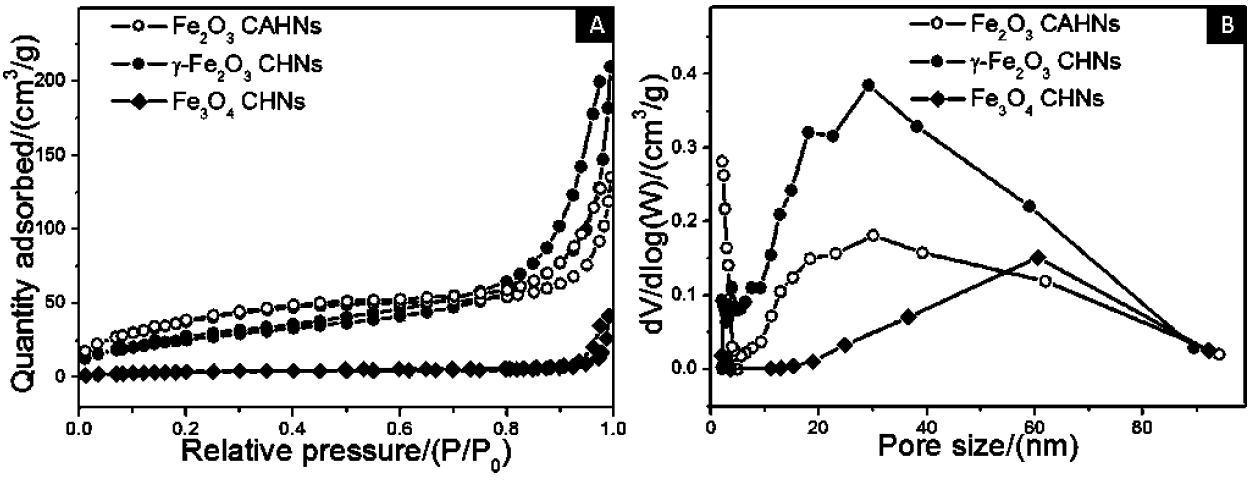

Figure 6. Nitrogen adsorption−desorption isotherms (A) and pore-size distribution curves (B) of the Fe_2O_3 CAHNs, γ-Fe_2O_3, and Fe_3O_4 CHNs, respectively.

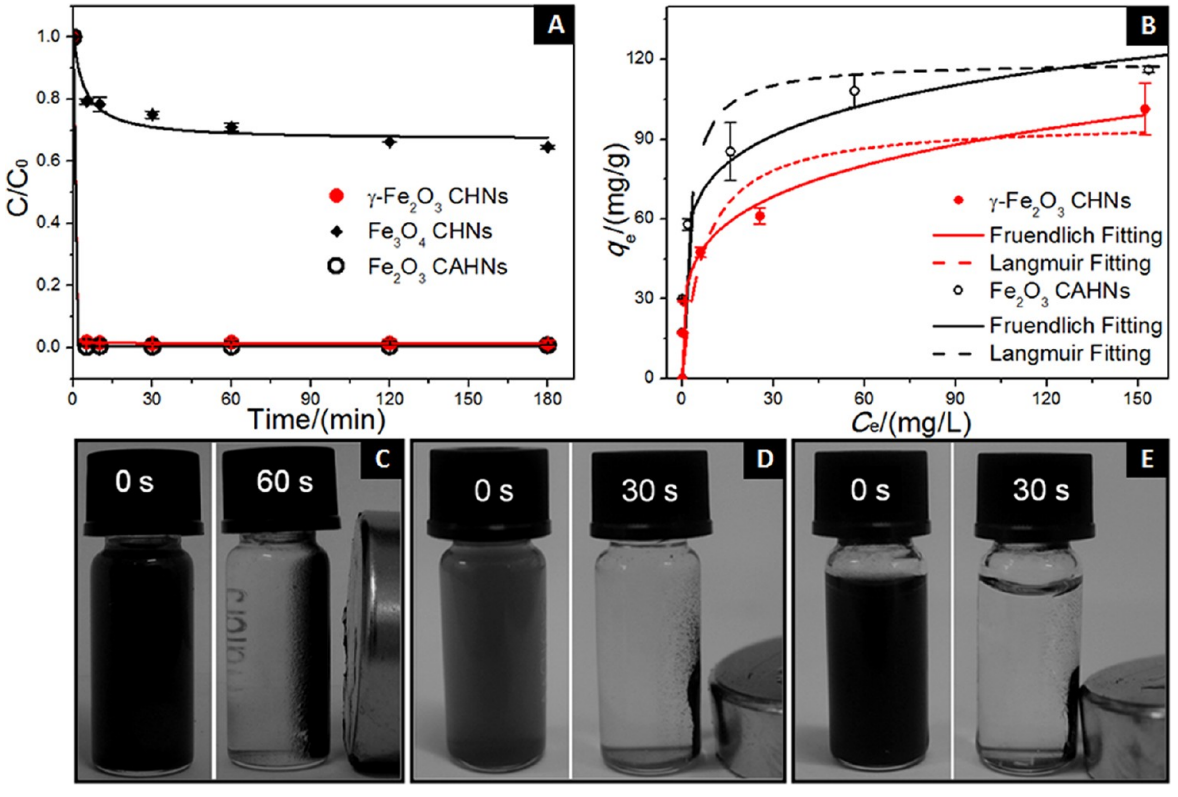

Figure 7. (A) Kinetics of As(V) adsorption on the Fe_2O_3 CAHNs, γ-Fe_2O_3, and Fe_3O_4 CHNs for a polluted solution with As(V) of 6.96 mg·$L^{-1}$and pH of 4. (B) Equilibrium isotherm data of As(V) adsorption on the Fe_2O_3 CAHNs and γ-Fe_2O_3 CHNs at pH = 4 and room temperature, as well as the nonlinear isotherm analysis using both Langmuir and Freundlich adsorption equations; Magnetic separation of the Fe_2O_3 CAHNs (C), γ-Fe_2O_3 CHNs (D), and Fe_3O_4 CHNs (E) from the treated As(V) solutions by a magnet with a magnetic field intensity of 3350 G on the flat surface and 1130 G on the cylindrical surface.

disorder, stoichiometric deviation, cation distribution and adsorbed species.[30,31] The inset of Figure 5 displays the zoom region between −400 and 400 Oe to show the hysteresis loops more clearly. It indicates that the H_c and M_r of the as-obtained γ-Fe_2O_3 CHNs (26 Oe and 0.57 emu·g^{-1}) are both lower than those of Fe_3O_4 CHNs (176.7 Oe and 15.1 emu·g^{-1}).

To further investigate the influence of calcination temperature (T) on the microstructure of the chestnutlike hierarchical structures and evaluate its expected high surface area because of the hierarchical and porous structure, we performed the analysis of the Brunauer−Emmett−Teller specific surface area (S_{BET}) and corresponding nitrogen adsorption and desorption isotherms. The S_{BET} of the Fe_2O_3 CAHNs is 143.12 m^2 g^{-1}, while that of the γ-Fe_2O_3 and Fe_3O_4 CHNs obtained at 300 and 500 °C is 96.44 and 14.90 m^2g^{-1}, respectively. This indicates that T has a great negative influence on S_{BET}. However, the S_{BET} of the as-obtained γ-Fe_2O_3 CHNs is still bigger than that of the hierarchically α-Fe_2O_3 hollow spheres (12.2 m^2·g^{-1}),[32] and α-Fe_2O_3 (40 m^2·g^{-1}), γ-Fe_2O_3 (56 m^2·g^{-1}), and Fe_3O_4 (34 m^2·g^{-1}) flowerlike nanostructures.[22] The nitrogen adsorption

and desorption isotherms of the γ-Fe_2O_3 and Fe_3O_4 CHNs are consistent with the characteristic of a type IV isotherm with a type H3 hysteresis loop associated with slit-like pores, as shown in Figure 6A. This indicates the presence of mesopores in the size range 2−50 nm.[33] In addition, the observed hysteresis loop shifts to a higher relative pressure of $P/P_0 = 1$, suggesting the presence of macropores (>50 nm in size).[34] These features could be further confirmed by wide pores size distribution of the samples (Figure 6B). The pore size distribution analysis also shows a great influence of T on the microstructure. The pore size distribution curve of the Fe_2O_3 CAHNs shows a sharp peak in the range of 2−6 nm and a broad peak ranging from the mesopore diameters of about 6 nm to the macropore diameters of 100 nm. For the γ-Fe_2O_3 CHNs obtained at 300 °C, the pore size is mainly located in the range of 6−100 nm, and the pores of less than 6 nm in size drop dramatically. The pores of less than 20 nm in size could not be observed in the Fe_3O_4 CHNs obtained at 500 °C, which only show a broad peak at diameters of 60 nm. The decreasing S_{BET} and loss of small-size pores may be associated with the collapse of mesopores under the high temperature calcination.[33]

Because of the high S_{BET} and good magnetic properties, the as-obtained γ-Fe_2O_3 CHNs are promising for water treatment. Figure 7A shows the kinetics of As(V) adsorption onto the Fe_2O_3 CAHNs, γ-Fe_2O_3, and Fe_3O_4 CHNs. Similar to the Fe_2O_3 CAHNs, the γ-Fe_2O_3 CHNs remove As(V) almost completely in 30 min. However, the Fe_3O_4 CHNs remove only 35.4% of As(V) from the polluted water even at 180 min. The As(V) removal capacity of the Fe_3O_4 CHNs herein is calculated to be 6.07 $mg{\cdot}g^{-1}$ (C_e = 4.52 $mg{\cdot}L^{-1}$), which is lower than that of most of the other magnetic adsorbents shown in Table 1. The low As(V) adsorption rate and capacity on the Fe_3O_4 CHNs can be ascribed to the low S_{BET} of 14.90 $m^2{\cdot}g^{-1}$.

Table 1. BET Specific Surface Area and the Maximal As(V) Adsorption Capacity (Q_m) of the As-Obtained Samples and Other Magnetic Adsorbents

adsorbents	S_{BET} ($m^2{\cdot}g^{-1}$)	Q_m ($mg{\cdot}g^{-1}$)	pH	ref
γ-Fe_2O_3 CHNs	96.44	101.4	4	this study
Fe_3O_4 CHNs	14.90	6.07[a]	4	this study
Fe_2O_3 CAHNs	143	137.5	4	23
γ-Fe_2O_3 nanoparticles	203	50	3	12
γ-Fe_2O_3 flowers	56	4.75	4	22
Fe_3O_4 nanoparticles	98.8	46.7	8	13
$MnFe_2O_4$ nanoparticles	138	90.4	3	38
Fe_3O_4/BN	218.6	32.18	6.9	40

[a]Data from kinetic study.

To evaluate the As(V) adsorption capacity of the as-obtained γ-Fe_2O_3 CHNs, the adsorption isotherm was conducted, as shown as dots in Figure 7B. The amount of As(V) adsorbed on the as-obtained γ-Fe_2O_3 CHNs at equilibrium (q_e) increases with increasing C_e, and is not saturated even when C_e = 152 $mg{\cdot}L^{-1}$. The maximal As(V) removal capacity (Q_m) is as high as 101.4 $mg{\cdot}g^{-1}$ within our experimental range (Figure 7B). This value is higher than that of the other magnetic adsorbents shown in Table 1 but slightly lower than that of the Fe_2O_3 CAHNs. Furthermore, compared to the conventional non-magnetic adsorbents, the as-prepared γ-Fe_2O_3 CHNs also show a superior As(V) adsorption capacity. For instance, Q_m of the activated alumina is 9.20 at pH = 7,[35] while that of the activated carbon with different carbon type and ash content were 2.4−4.9 $mg{\cdot}g^{-1}$ at pH = 5.[36] For TiO_2 nanoparticles, Q_m = 37.5 $mg{\cdot}g^{-1}$ at pH = 7.[37] Generally, the large S_{BET} is mainly responsible for the strong adsorption behavior of metal oxides. Table 1 shows that $MnFe_2O_4$, Fe_3O_4 and maghemite nanoparticles exhibit a much lower Q_m than the as-prepared γ-Fe_2O_3 CHNs even though they both have a similar or higher S_{BET} than the latter.[12,13,38] This reasonably suggests that the high S_{BET} is not the only criterion for the strong As(V) adsorption capacities, which are sometimes intensively influenced by the surface quality or surface property. In our protocol, the as-obtained γ-Fe_2O_3 CHNs obviously have numerous nanoparticles in core and nanorods in shell, which form a heterogeneous surface. This possibly results in a multilayer As(V) adsorption behavior and consequently a superior adsorption capacity. But the nanoparticles of $MnFe_2O_4$ and maghemite have only a homogeneous surface, which usually shows a monolayer adsorption behavior of the Langmuir isotherm model.[12,13,38] Thus they show a weaker adsorption capability for As(V) than the as-obtained γ-Fe_2O_3 CHNs even though they have a similar or higher S_{BET} compared to the as-prepared γ-Fe_2O_3 CHNs.[39]

To further understand the adsorption mechanism of the as-prepared γ-Fe_2O_3 CHNs as an adsorbent, both the Langmuir adsorption model and the Freundlich adsorption model[41] were employed to fit the experimental data, as shown in Figure 7B. The detailed Langmuir and Freundlich isotherm parameters are summarized in Table 2. The experimental data fit well to the

Table 2. Related Parameters of Both the Langmuir and Freundlich Isotherm Models for As(V) Equilibrium Adsorption on the γ-Fe_2O_3 CHNs at pH = 4 and Room Temperature

isotherm equation	different parameters	estimated parameters
Freundlich model	R^2	0.991
$q_e = K_F C_e^{(1/n)}$	K_F	31.54
	n	4.39
Langmuir model	R^2	0.775
$q_e = (q_m b C_e)/(1 + bC_e)$	q_m ($mg{\cdot}g^{-1}$)	96.80
	b ($mg{\cdot}L^{-1}$)	0.14

Freundlich adsorption model rather than the Langmuir adsorption model. The regression coefficient (R^2) for the Freundlich adsorption model is 0.991, higher than that of Langmuir adsorption model (0.775). This suggests that the As(V) adsorption behavior of the γ-Fe_2O_3 CHNs can be regarded as a multilayer adsorption process, and the Langmuir adsorption model is not suitable for describing it. This is because the Langmuir isotherm model assumes that homogeneous surfaces, in which all sites are energetically equivalent, adsorb adsorbates only in a monolayer way and that there is no interaction between the adsorbed molecules. In contrast, the Freundlich isotherm model is an empirical equation based on the multilayer adsorption on heterogeneous surfaces. The stronger binding sites are first occupied by the adsorbates. The binding strength decreases gradually with increasing the occupied sites.[41] Since the as-obtained γ-Fe_2O_3 CHNs consist of numerous nanoparticles in core and nanorods in shell, it is imaginable that they have heterogeneous surfaces. Specifically, the surface properties differ from the various nanoparticles of the interior core because of their different exposed lattice surfaces, as well as those between the γ-Fe_2O_3 nanoparticles and nanorods. Thus, the surface heterogeneities of the γ-Fe_2O_3

dx.doi.org/10.1021/am300814q | ACS Appl. Mater. Interfaces 2012, 4, 3987−3993

CHNs lead to different affinities to As(V) at different sites. Consequently, the As(V) adsorption behavior of the γ-Fe_2O_3 CHNs obeys the Freundlich adsorption model well. This further confirms the assumption that multilayered adsorption occurs in the γ-Fe_2O_3 CHNs.

The equilibrium isotherm data of As(V) adsorption on the Fe_2O_3 CAHNs and the corresponding Langmuir and Freundlich fitting curves are also shown in Figure 7B, indicating the adsorption of As(V) on Fe_2O_3 CAHNs also obeys the Freundlich adsorption model well. Hence, the lower As(V) adsorption capacity of the as-obtained γ-Fe_2O_3 CHNs (101.4 $mg{\cdot}g^{-1}$) comparing to that of the Fe_2O_3 CAHNs (137.5 $mg{\cdot}g^{-1}$) can be mainly ascribed to the decreasing S_{BET} in the calcination (S_{BET} = 143 $m^2{\cdot}g^{-1}$ for the Fe_2O_3 CAHNs, while S_{BET} = 96.44 $m^2{\cdot}g^{-1}$ for the γ-Fe_2O_3 CHNs).

The Freundlich sorption coefficient (K_F) is 31.54 $(mg{\cdot}g^{-1})$-$(L{\cdot}mg^{-1})^{1/n}$ for the As(V) adsorption on the as-obtained γ-Fe_2O_3 CHNs, which is much higher than that of granular ferric hydroxide (4.45),[42] nanocrystalline TiO_2 (0.5−0.75),[43] iron coated pottery granules (3.6),[44] and tea fungal biomass (10.26).[45] This indicates the as-obtained γ-Fe_2O_3 CHNs has a larger overall capacity.[46] However, K_F for the As(V) adsorption on the as-obtained γ-Fe_2O_3 CHNs is lower than that of the Fe_2O_3 CAHNs (46.86),[23] indicating the as-obtained γ-Fe_2O_3 CHNs have a lower As(V) adsorption overall capacity. $0.1 < 1/n \leq 0.5$ represents the easy adsorption, and $0.5 < 1/n \leq 1$ represents the somewhat difficult adsorption; and $1/n > 1$ represents the quite difficult adsorption.[47] For the removal of As(V) from polluted water by the γ-Fe_2O_3 CHNs, $1/n = 0.228$. This indicates that As(V) ions are easily adsorbed on the as-obtained γ-Fe_2O_3 CHNs.

Thanks to the fine magnetic properties, the as-obtained γ-Fe_2O_3 CHNs can be conveniently separated from the As(V) solution in 30 s by a magnet, as shown in Figure 7D, which is quicker even with a lower magnetic field than the magnetic separation of the Fe_2O_3 CAHNs (60 s, Figure 7C). The quicker magnetic separation of the as-obtained γ-Fe_2O_3 CHNs is attributed to their enhanced M_s because the weak ferromagnetic amorphous core of the Fe_2O_3 CAHNs are crystallized into the strong ferromagnetic maghemite by a subsequent heat treatment. Figure 7E shows that the as-obtained Fe_3O_4 CHNs can also be conveniently separated from the As(V) solution in 30 s after the treatment is completed.

CONCLUSION

In summery, we have successfully prepared strong magnetic γ-Fe_2O_3 and Fe_3O_4 chestnutlike hierarchical nanostructures (CHNs) by annealing the Fe_2O_3 chestnut-like amorphous core/γ-phase shell hierarchical nanoarchitectures (CAHNs) at elevated temperatures under a nitrogen atmosphere. The as-obtained γ-Fe_2O_3 CHNs have an extraordinary high As(V) removal capacity of 101.4 $mg{\cdot}g^{-1}$. The As(V) adsorption process obeys well the Freundlich isotherm model rather than the Langmuir one, suggesting the occurrence of a multilayered adsorption on the surface of the γ-Fe_2O_3 CHNs. Taking advantages of the high adsorption capacity, rapid adsorption rate and quick magnetic separation from the treated water, the γ-Fe_2O_3 CHNs developed in present study can be regarded as an ideal magnetic adsorbent for As(V) removal from aqueous solutions.

AUTHOR INFORMATION

Corresponding Author

*E-mail: guanjg@whut.edu.cn.

Notes

The authors declare no competing financial interest.

ACKNOWLEDGMENTS

This work was supported by the National Natural Science Foundation of China (51002111), the Natural Science Foundation of Hubei Province (2010CDA030 and 2010CDB00606), the Subject Leadership Project of Wuhan City (201150530145), the Fundamental Research Funds for the Central Universities (No. 2011-Ia-013 and 2012-IV-085), and Postdoctoral Science Foundation of China (No. 20100471163 and 201104494).

REFERENCES

(1) Karim, M. *Water Res.* **2000**, *34*, 304.
(2) Chakraborti, D.; Rahman, M. M.; Paul, K.; Chowdhury, U. K.; Sengupta, M. K.; Lodh, D.; Chanda, C. R.; Saha, K. C.; Mukherjee, S. C. *Talanta* **2002**, *58*, 3.
(3) Mohan, D.; Pittman, C. U. *J. Hazard. Mater.* **2007**, *142*, 1.
(4) Gihring, T. M.; Druschel, G. K.; McCleskey, R. B.; Hamers, R. J.; Banfield, J. F. *Environ. Sci. Technol.* **2001**, *35*, 3857.
(5) Zaw, M.; Emett, M. T. *Toxicol. Lett.* **2002**, *133*, 113.
(6) Meng, X. G.; Korfiatis, G. P.; Bang, S. B.; Bang, K. W. *Toxicol. Lett.* **2002**, *133*, 103.
(7) Pattanayak, J.; Mondal, K.; Mathew, S.; Lalvani, S. B. *Carbon* **2000**, *38*, 589.
(8) Lin, T. F.; Wu, J. K. *Water Res.* **2001**, *35*, 2049.
(9) Kim, J.; Benjamin, M. M. *Water Res.* **2004**, *38*, 2053.
(10) Yavuz, C. T.; Mayo, J. T.; Yu, W. W.; Prakash, A.; Falkner, J. C.; Yean, S.; Cong, L. L.; Shipley, H. J.; Kan, A.; Tomson, M.; Natelson, D.; Colvin, V. L. *Science* **2006**, *314*, 964.
(11) Polshettiwar, V.; Luque, R.; Fihri, A.; Zhu, H.; Bouhrara, M.; Basset, J. M. *Chem. Rev.* **2011**, *111*, 3036.
(12) Tuutijarvi, T.; Lu, J.; Sillanpaa, M.; Chen, G. *J. Hazard. Mater.* **2009**, *166*, 1415.
(13) Yean, S.; Cong, L.; Yavuz, C. T.; Mayo, J. T.; Yu, W. W.; Kan, A. T.; Colvin, V. L.; Tomson, M. B. *J. Mater. Res.* **2005**, *20*, 3255.
(14) Wang, P.; Lo, I. M. C. *Water Res.* **2009**, *43*, 3727.
(15) Tong, G. X.; Guan, J. G.; Xiao, Z. D.; Mou, F. Z.; Wang, W.; Yan, G. Q. *Chem. Mater.* **2008**, *20*, 3535.
(16) Mou, F. Z.; Guan, J. G.; Sun, Z. G.; Fan, X. A.; Tong, G. X. *J. Solid State Chem.* **2010**, *183*, 736.
(17) Tong, G. X.; Guan, J. G.; Xiao, Z. D.; Huang, X.; Guan, Y. *J. Nanopart. Res.* **2010**, *12*, 3025.
(18) Liu, L. J.; Guan, J. G.; Shi, W. D.; Sun, Z. G.; Zhao, J. S. *J. Phys. Chem. C* **2010**, *114*, 13565.
(19) Hu, J. S.; Zhong, L. S.; Song, W. G.; Wan, L. J. *Adv. Mater.* **2008**, *20*, 2977.
(20) Liang, X.; Xi, B. J.; Xiong, S. L.; Zhu, Y. C.; Xue, F.; Qian, Y. T. *Mater. Res. Bull.* **2009**, *44*, 2233.
(21) Qiu, G.; Huang, H.; Genuino, H.; Opembe, N.; Stafford, L.; Dharmarathna, S.; Suib, S. L. *J. Phys. Chem. C* **2011**, *115*, 19626.
(22) Zhong, L. S.; Hu, J. S.; Liang, H. P.; Cao, A. M.; Song, W. G.; Wan, L. J. *Adv. Mater.* **2006**, *18*, 2426.
(23) Mou, F. Z.; Guan, J. G.; Xiao, Z. D.; Sun, Z. G.; Shi, W. D.; Fan, X. A. *J. Mater. Chem.* **2011**, *21*, 5414.
(24) Machala, L.; Zboril, R.; Gedanken, A. *J. Phys. Chem. B* **2007**, *111*, 4003.
(25) Legodi, M. A.; de Waal, D. *Dyes Pigm.* **2007**, *74*, 161.
(26) Chamritski, I.; Burns, G. *J. Phys. Chem. B* **2005**, *109*, 4965.
(27) Wang, Z. W.; Saxena, S. K. *Solid State Commun.* **2002**, *123*, 195.
(28) Dutta, P.; Manivannan, A.; Seehra, M. S.; Shah, N.; Huffman, G. P. *Phys. Rev. B* **2004**, *70*, 174428.

(29) Andrés-Vergés, M.; del Puerto Morales, M.; Veintemillas-Verdaguer, S.; Palomares, F. J.; Serna, C. J. *Chem. Mater.* **2011**, *24*, 319.
(30) Cabot, A.; Alivisatos, A. P.; Puntes, V. F.; Balcells, L.; Iglesias, Ò.; Labarta, A. *Phys. Rev. B* **2009**, *79*, 094419.
(31) Fan, X. a.; Guan, J.; Li, Z.; Mou, F.; Tong, G.; Wang, W. *J. Mater. Chem.* **2010**, *20*, 1676.
(32) Cao, S. W.; Zhu, Y. J. *J. Phys. Chem. C* **2008**, *112*, 6253.
(33) Sing, K. S. W.; Everett, D. H.; Haul, R. A. W.; Moscou, L.; Pierotti, R. A.; Rouquerol, J.; Siemieniewska, T. *Pure Appl. Chem.* **1984**, *57*, 603.
(34) Bavykin, D. V.; Parmon, V. N.; Lapkin, A. A.; Walsh, F. C. *J. Mater. Chem.* **2004**, *14*, 3370.
(35) Takanashi, H.; Tanaka, A.; Nakajima, T.; Ohki, A. *Water Sci. Technol.* **2004**, *50*, 23.
(36) Lorenzen, L.; van Deventer, J. S. J.; Landi, W. M. *Miner. Eng.* **1995**, *8*, 557.
(37) Pena, M. E.; Korfiatis, G. P.; Patel, M.; Lippincott, L.; Meng, X. G. *Water Res.* **2005**, *39*, 2327.
(38) Zhang, S. X.; Niu, H. Y.; Cai, Y. Q.; Zhao, X. L.; Shi, Y. L. *Chem. Eng. J.* **2010**, *158*, 599.
(39) Zhang, G. S.; Qu, J. H.; Liu, H. J.; Cooper, A. T.; Wu, R. C. *Chemosphere* **2007**, *68*, 1058.
(40) Chen, R.; Zhi, C.; Yang, H.; Bando, Y.; Zhang, Z.; Sugiur, N.; Golberg, D. *J. Colloid Interface Sci.* **2011**, *359*, 261.
(41) Bayramoglu, G.; Denizli, A.; Bektas, S.; Yakup Arica, M. *Microchem. J.* **2002**, *72*, 63.
(42) Badruzzaman, M.; Westerhoff, P.; Knappe, D. R. U. *Water Res.* **2004**, *38*, 4002.
(43) Bang, S.; Patel, M.; Lippincott, L.; Meng, X. G. *Chemosphere* **2005**, *60*, 389.
(44) Dong, L. J.; Zinin, P. V.; Cowen, J. P.; Ming, L. C. *J. Hazard. Mater.* **2009**, *168*, 626.
(45) Murugesan, G. S.; Sathishkumar, M.; Swaminathan, K. *Bioresour. Technol.* **2006**, *97*, 483.
(46) Droste, R. L. *Theory and Practice of Water and Wastewater Treatment*; John Wiley and Sons, Inc.: New York, 1997.
(47) Treybal, R. E. *Mass-Transfer Operations*, 3rd ed.; McGraw-Hill international: Singapore, 1981.